Photocatalysis
Research and Potential

SciEPublish

Article

CoPi Cocatalyst-Decorated TiO_2/NiO Nanotube Heterojunction Photoanode for Enhanced Photoelectrochemical Performance

Shouyun Zhang [1], Hongjin Chang [1], Dongyu Mei [1], Xu Liu [1], Fujian Lv [2,*], Zhao Wang [3], Qinrong Kang [4] and Ling Wu [1,*]

[1] Hubei Province Key Laboratory of Coal Conversion and New Carbon Materials, School of Chemistry and Chemical Engineering, Wuhan University of Science and Technology, Wuhan 430081, China; zsy666@wust.edu.cn (S.Z.); Jin426711@wust.edu.cn (H.C.); MDY0924@wust.edu.cn (D.M.); Liu0387@wust.edu.cn (X.L.)

[2] College of Chemistry and Environmental Science, Qujing Normal University, Qujing 655400, China

[3] Hubei Provincial Engineering Research Center of Racing Horse Detection and Application Transformation, Equine Science Research and Horse Doping Control Laboratory, Wuhan Business University, Wuhan 430056, China; wangzhao517@stu.hubu.edu.cn (Z.W.)

[4] School of Resources and Safety Engineering, Wuhan Institute of Technology, Wuhan 430074, China; 12060101@wit.edu.cn (Q.K.)

* Corresponding author. E-mail: lvfujian@mail.qjnu.edu.cn (F.L.); wuling2018@wust.edu.cn (L.W.)

Received: 15 September 2026; Revised: 16 October 2026; Accepted: 2 November 2026; Available online: 16 November 2026

ABSTRACT: Photoelectrochemical (PEC) water splitting is promising for solar-to-hydrogen conversion, but its efficiency is limited by sluggish oxygen evolution reaction (OER) kinetics and severe charge recombination at the photoanode. Constructing heterojunctions with oxygen evolution cocatalysts is an effective strategy to overcome these limitations. Herein, a CoPi cocatalyst-decorated TiO_2/NiO heterojunction photoanode (TNC) was fabricated by anodization of Ti sheets, NiO electrodeposition, and CoPi photodeposition. Characterization confirmed the successful anchoring of cubic NiO nanoparticles on anatase TiO_2 nanotube arrays and the homogeneous deposition of amorphous CoPi on the TiO_2/NiO surface. The resulting TNC photoanode exhibited extended visible-light absorption from 400 to 800 nm, efficient charge separation, and excellent PEC performance. Compared with pristine TiO_2 and TiO_2/NiO, TNC delivered the highest photocurrent density, the smallest charge-transfer resistance, the most negative open-circuit potential, and the shortest carrier decay lifetime. The enhanced PEC performance is attributed to the TiO_2/NiO heterojunction, which promotes charge separation, and the CoPi layer, which acts as a hole-extraction layer, passivates surface trap states, and accelerates interfacial hole transfer for water oxidation. This work provides a rational strategy for constructing efficient multi-component photoanodes for solar water splitting.

Keywords: TiO_2 nanotube arrays; Heterojunction; CoPi cocatalyst; Photodeposition

© 2026 The authors. This is an open access article under the Creative Commons Attribution 4.0 International License (https://creativecommons.org/licenses/by/4.0/).

1. Introduction

Solar-driven photoelectrochemical (PEC) water splitting is one of the most promising strategies for converting intermittent solar energy into clean, storable hydrogen fuel. However, its practical efficiency is largely limited by the photoanode, where the oxygen evolution reaction (OER) suffers from sluggish four-electron kinetics and severe charge recombination [1–3]. Among various photoanode materials, TiO_2 nanotube arrays have attracted extensive attention because of their low cost, non-toxicity, high chemical stability, large specific surface area, and efficient one-dimensional charge transport [4–6]. TiO_2 nanotube arrays have been widely applied in photocatalytic pollutant degradation [5,7–9], photocatalytic CO_2 reduction [10–12], and photocatalytic water splitting [13]. Nevertheless, pristine TiO_2 nanotube arrays suffer from a wide band gap (~3.2 eV for anatase), which restricts their photoresponse mainly to the ultraviolet region of the solar spectrum. Moreover, as with many semiconductors, the photogenerated carriers in TiO_2 nanotube arrays are prone to recombination, which severely limits their further application in photocatalysis and PEC water splitting [14].

Constructing heterojunctions is an effective strategy to overcome these limitations. In our previous studies, CdS quantum dots decorated on TiO_2 nanotube arrays formed TiO_2/CdS heterojunctions, enabling efficient photoelectrocatalytic degradation of methyl orange under visible-light irradiation [15]. Similarly, Au nanoparticles loaded on TiO_2 nanotube arrays constructed plasmonic TiO_2/Au heterostructures, which achieved effective visible-light PEC removal of organic pollutants via plasmon-induced charge separation [16]. These results indicate that heterojunction construction and interfacial modification are feasible routes to enhance the PEC performance of TiO_2 nanotube arrays [17,18]. However, CdS suffers from photocorrosion, and Au is costly and scarce; moreover, both systems were designed for pollutant degradation rather than solar water oxidation. Therefore, developing stable, low-cost, and efficient TiO_2 nanotube arrays-based photoanodes for PEC water oxidation remains highly desirable. Nickel oxide (NiO) is a promising p-type semiconductor because of its excellent stability, low cost, high hole mobility, and visible-to-near-infrared light absorption, which can significantly improve the full-spectrum light harvesting of TiO_2 nanotube arrays-based electrodes [19]. Accordingly, TiO_2/NiO heterostructures have been constructed as a means to extend visible-light absorption and promote charge separation, mostly in photocatalytic and photoelectrocatalytic degradation. For example, Parvizi et al. electrodeposited NiO on TiO_2 nanotube arrays, extending absorption to 200–800 nm and improving the PEC degradation of Acid Blue 113 [20]. Liu et al. loaded black NiO nanoclusters on TiO_2 nanorods, where the heterojunction enhanced carrier separation and suppressed recombination, enabling better photocatalytic degradation performance than bare TiO_2 and NiO [21].

Although these studies demonstrate that TiO_2/NiO heterostructures can enhance light absorption and charge separation, they still face critical challenges for PEC water oxidation. The OER is a four-electron process with sluggish kinetics and a high overpotential [22]. Photogenerated holes accumulated at the NiO surface may recombine before driving water oxidation, and surface trap states can capture charge carriers and hinder interfacial hole transfer [23]. Consequently, the PEC performance of TiO_2/NiO photoanodes remains limited by inefficient surface water oxidation. Loading an oxygen evolution cocatalyst is an effective strategy to overcome these limitations. Among various cocatalysts, cobalt phosphate (CoPi) is particularly attractive because of its earth abundance, low cost, and self-healing property [14,24,25]. CoPi can act as a hole extraction layer to promote interfacial hole transfer and improve water oxidation kinetics, as demonstrated on photoanodes such as $BiVO_4$ [26] and α-Fe_2O_3 [27]. Therefore, integrating CoPi with a TiO_2/NiO heterostructure is expected to synergistically enhance charge separation and water oxidation.

Despite the individual benefits of TiO_2/NiO heterostructures and CoPi cocatalysts, the rational integration of both components on TiO_2 nanotube arrays for enhanced PEC water oxidation remains attractive and needs further exploration. Herein, we report a CoPi cocatalyst-decorated TiO_2/NiO

heterostructured photoanode (TNC) for enhanced PEC water oxidation. The TNC photoanode was fabricated by two-step anodic oxidation of Ti sheets to form TiO_2 nanotube arrays, followed by electrodeposition and annealing of NiO nanoparticles and subsequent photodeposition of CoPi. The morphology, crystal structure, surface chemical states, optical absorption, and semiconductor characteristics were systematically characterized. Its PEC performance was evaluated by transient photocurrent, linear sweep voltammetry (LSV), electrochemical impedance spectroscopy (EIS), and open-circuit potential (OCP) decay measurements. The TNC photoanode exhibits the highest photocurrent density, the smallest charge-transfer resistance, the most negative OCP, and the shortest carrier decay lifetime compared with the pristine TiO_2 nanotube arrays and the TiO_2/NiO heterostructure. This work demonstrates that the TiO_2/NiO heterointerface, together with the CoPi cocatalyst, synergistically enhances charge separation, interfacial hole transfer, and PEC performance, providing a rational design strategy for efficient multi-component photoanodes.

2. Materials and Methods

2.1. Preparation of T/NiO/CoPi Photoanode

As schematically illustrated in Figure 1, the T/NiO/CoPi photoanode was fabricated through a three-step route consisting of two-step anodization of Ti sheets, NiO electrodeposition, and CoPi photodeposition. The materials and reagents used are listed in the Supporting Information (Text S1). First, TiO_2 nanotube arrays were fabricated on Ti sheets via a two-step anodic oxidation method. Prior to anodization, Ti sheets (2 cm × 3.5 cm, 0.1 mm thickness, purity > 99.9%) were sequentially ultrasonically cleaned in ethanol and deionized (DI) water for 10 min. A cleaned Ti sheet was used as the working electrode, a Pt sheet as the counter electrode, and an ethylene glycol solution containing 0.3 wt% NH_4F and 2.0 vol% DI water as the electrolyte. The first anodic oxidation was conducted at 30 V for 2 h. The as-anodized sample was then ultrasonically cleaned for 10 min to remove the oxide film on the Ti sheet surface, followed by a second anodization under the same conditions for 3 h. After anodization, it was rinsed with ethanol and DI water and dried at room temperature. Finally, the dried electrode was calcined in a muffle furnace at 500 °C for 2 h with a heating rate of 2 °C·min^{-1} to obtain crystalline TiO_2 nanotube arrays (denoted as T).

NiO nanoparticles (NPs) were electrodeposited onto TiO_2 nanotube arrays using a standard three-electrode configuration, with Ni sheet as the working electrode, the as-prepared T as the counter electrode, and Ag/AgCl (saturated KCl) as the reference electrode. The Ni sheet was pretreated in the same manner as the Ti sheet. An electrolyte was prepared by mixing equal volumes of 67.3 g·L^{-1} $NiSO_4$, 22.5 g·L^{-1} $NiCl_2$, and 18.5 g·L^{-1} H_3BO_3, and its pH was adjusted to 4.5 with 0.01 M HCl. A constant current of 5 mA was applied for 3 min to control the NiO loading. The resulting electrode was annealed in a muffle furnace at 400 °C for 4 h at a heating rate of 2 °C·min^{-1} to convert the deposited Ni into NiO, yielding the T/NiO electrode (denoted as TN). CoPi cocatalyst was loaded onto TN by a photodeposition method [28,29]. TN was immersed in a mixed solution of 0.5 mM $Co(NO_3)_2$ and 0.025 M phosphate buffer solution (0.025 M Na_2HPO_4 and 0.025 M NaH_2PO_4, pH ≈ 7), and irradiated under AM 1.5 illumination (100 mW·cm^{-2}) for 90 s to obtain T/NiO/CoPi photoanode (denoted as TNC).

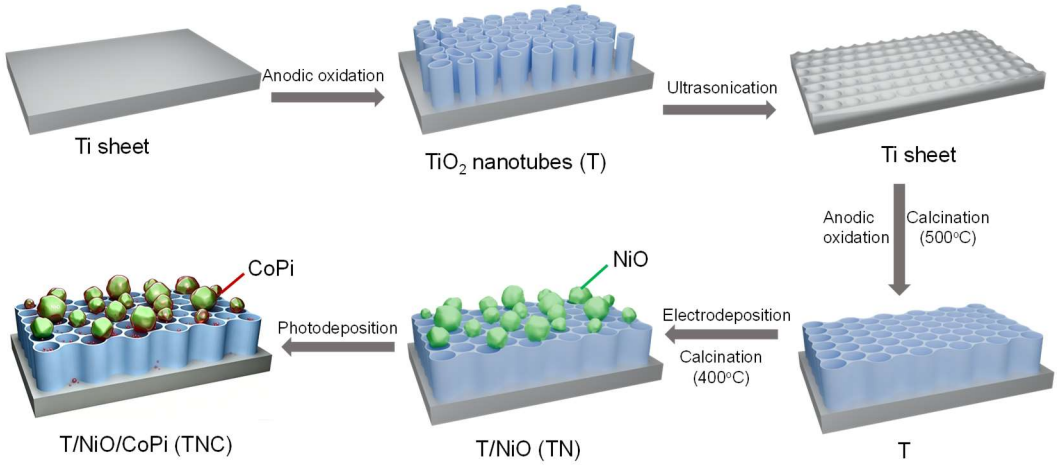


Figure 1. Schematic illustration for the fabrication process of the TNC photoanode.

2.2. Electrode Characterizations

The morphology of the as-fabricated electrodes was investigated using a field emission scanning electron microscope (SEM, JSM-7610F Plus, JEOL, Tokyo, Japan) and transmission electron microscope (JEM-F200, JEOL, Tokyo, Japan). The crystalline phase was characterized by an X-ray powder diffractometer (XRD, SmartLab SE, Rigaku Corporation, Tokyo, Japan) with Cu K_α radiation. The surface chemical states were analyzed by X-ray photoelectron spectroscopy (XPS, PHI 5000, ULVAC-PHI, Chigasaki, Japan). All the binding energy values were calibrated using C 1s (284.6 eV) as a reference. The diffuse reflectance spectra (DRS) over a range of 200–800 nm were recorded by a UV-2550 spectrophotometer (UV-2550, Shimadzu Corporation, Kyoto, Japan) with an integrating sphere. The characterization details are provided in Text S2.

2.3. Photoelectrochemical Measurements

All photoelectrochemical measurements were conducted on an electrochemical station (CHI760E, Shanghai Chenhua Instrument Co., Ltd., Shanghai, China) in a three-electrode cell. A Pt sheet was utilized as the counter electrode, an Ag/AgCl (saturated KCl) electrode as the reference electrode, and the as-fabricated photoanode (T, TN or TNC) as the working electrode. A xenon lamp (CEL-PE300-4A, Beijing China Education Au-light Co., Ltd., Beijing, China) was employed as the light source to provide simulated solar illumination (AM 1.5G, 100 $mW \cdot cm^{-2}$), which was uniformly and parallelly irradiated onto the front side of these electrodes. All PEC tests were carried out in a 0.1 M Na_2SO_4 solution. Mott–Schottky plots were recorded in the dark at 1000 Hz with an amplitude of 5 mV over a potential range from −0.2 to 1.65 V *vs.* Ag/AgCl. Transient photocurrent–time (*I–t*) curves were recorded at a bias voltage of 0.6 V *vs.* Ag/AgCl under repeated light on-off cycles (30 s dark and 30 s light). OCP and EIS measurements were performed under open-circuit conditions. EIS was carried out over a frequency range of 100 kHz to 0.01 Hz with an amplitude of 5 mV. LSV was conducted under illumination at a scan rate of 5 $mV \cdot s^{-1}$, and the electrode potentials were converted to the reversible hydrogen electrode (RHE) using the Nernst equation.

3. Results and Discussion

3.1. Fabrication and Composition

The TNC photoanode was constructed by integrating a TiO_2 nanotube scaffold, NiO NPs, and a CoPi cocatalyst while preserving the one-dimensional nanotube architecture (Figure 1). The porous TiO_2 nanotube arrays were first formed by a two-step anodization strategy, in which the initial anodization layer was ultrasonically removed to leave ordered concave pits on the Ti substrate that served as favorable

nucleation templates for the subsequent anodization [30,31]. After secondary anodization and calcination at 500 °C, well-organized and tightly anchored porous TiO_2 nanotube arrays were obtained, providing an increased active surface area and improved electrical contact between TiO_2 and the underlying Ti sheet [30,32]. NiO NPs were then loaded on the TiO_2 surface via electrodeposition and calcination to prepare TN composites. Finally, the CoPi cocatalyst was immobilized on TN through photodeposition in Co^{2+}-containing phosphate buffer [33,34]. Under light irradiation, photogenerated holes on the TN photoanode oxidize Co^{2+} ions in the electrolyte to high-valence cobalt species, which spontaneously combine with phosphate anions and precipitate as amorphous CoPi cocatalyst on the electrode surface [35,36].

The XRD patterns of T, TN and TNC electrodes are shown in Figure 2a. For the bare T electrode, the peaks at 2θ = 40.2°, 53.0° and 70.7° originate from the Ti substrate (JCPDS No. 89-2959), while the typical anatase TiO_2 peaks, such as 25.3°, 37.8° and 48.7°, correspond to the (101), (004) and (200) planes (JCPDS No. 21-1272) [16]. No impurity peaks are observed, indicating high phase purity and good crystallinity. After NiO electrodeposition, TN exhibits an additional weak peak at 43.3°, which is indexed to the (200) plane of cubic NiO (JCPDS No. 75-0269) [37]. Following CoPi photodeposition, TNC electrode still exhibits the characteristic peaks of Ti, TiO_2 and NiO, but no peaks corresponding to crystalline CoPi, suggesting that the CoPi cocatalyst is amorphous or present at a loading below the XRD detection limit.

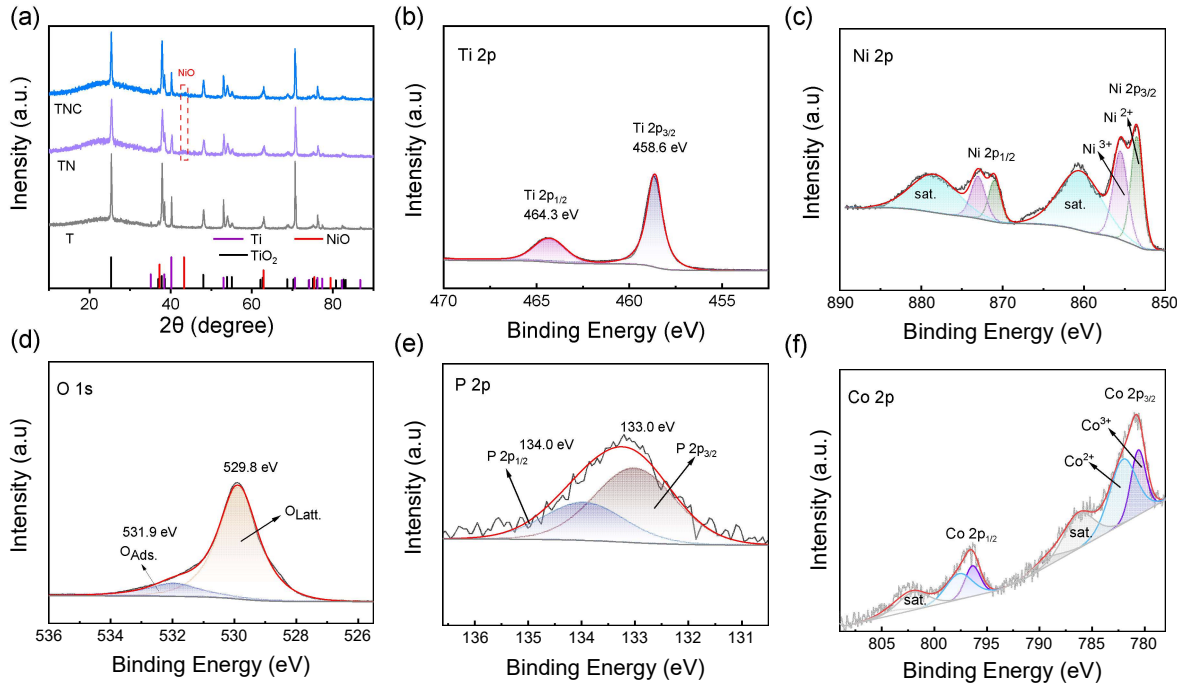


Figure 2. (**a**) XRD patterns of T, TN and TNC electrodes; High-resolution XPS spectra of TNC: (**b**) Ti 2p, (**c**) Ni 2p, (**d**) O 1s, (**e**) P 2p and (**f**) Co 2p.

The surface elemental composition and chemical states of TNC and TN were investigated by XPS. The Ti 2p spectra of both electrodes (Figures 2b and S1a) show two peaks at 458.6 and 464.3 eV, which are assigned to Ti $2p_{3/2}$ and Ti $2p_{1/2}$ of Ti^{4+} in TiO_2 [38], respectively. The Ni 2p spectra (Figures 2c and S1b) can be deconvoluted into Ni^{2+} (853.5 and 871.0 eV), Ni^{3+} (855.6 and 873.0 eV), and satellite peaks (860.7 and 878.8 eV), confirming the coexistence of Ni^{2+} and Ni^{3+} in NiO [39]. The O 1s spectra (Figures 2d and S1c) exhibit peaks at 529.8 and 531.9 eV, corresponding to lattice oxygen and surface hydroxyl/adsorbed oxygen species [40]. Notably, no obvious P or Co signals are detected in TN (Figure S1d,e). In contrast, the TNC electrode exhibits distinct P 2p peaks at 133.0 and 134.0 eV (Figure 2e), which are assigned to P $2p_{3/2}$ and P $2p_{1/2}$ of phosphate species, respectively [40]. In addition, the Co 2p spectrum of TNC (Figure 2f) can be fitted with Co^{3+} (780.7 and 796.4 eV), Co^{2+} (782.0 and 797.6 eV), and their associated satellite

peaks, confirming the presence of both Co^{3+} and Co^{2+} [41]. These results demonstrate the successful incorporation of phosphate and Co species into TNC.

3.2. Morphology and Nanostructure

The morphologies of T, TN, and TNC were examined by SEM, and the results are shown in Figure 3. As displayed in Figure 3a,a', T electrode prepared by two-step anodization exhibits highly ordered, densely packed, and smooth TiO_2 nanotube arrays with uniform pore openings. After NiO electrodeposition, the TN electrode (Figure 3b,b') shows NiO NPs distributed both on the nanotube surfaces and inside the nanotube arrays without severe particle agglomeration. TNC electrode (Figure 3c,c') maintains a morphology similar to that of TN, indicating that the CoPi cocatalyst is deposited without damaging the TiO_2/NiO nanotube architecture. The energy-dispersive X-ray spectroscopy (EDS) elemental mapping of TNC (Figure S2) clearly reveals the distribution of Ti, O, Ni, P, and Co, confirming the successful deposition of NiO and CoPi on the TiO_2 nanotube arrays.

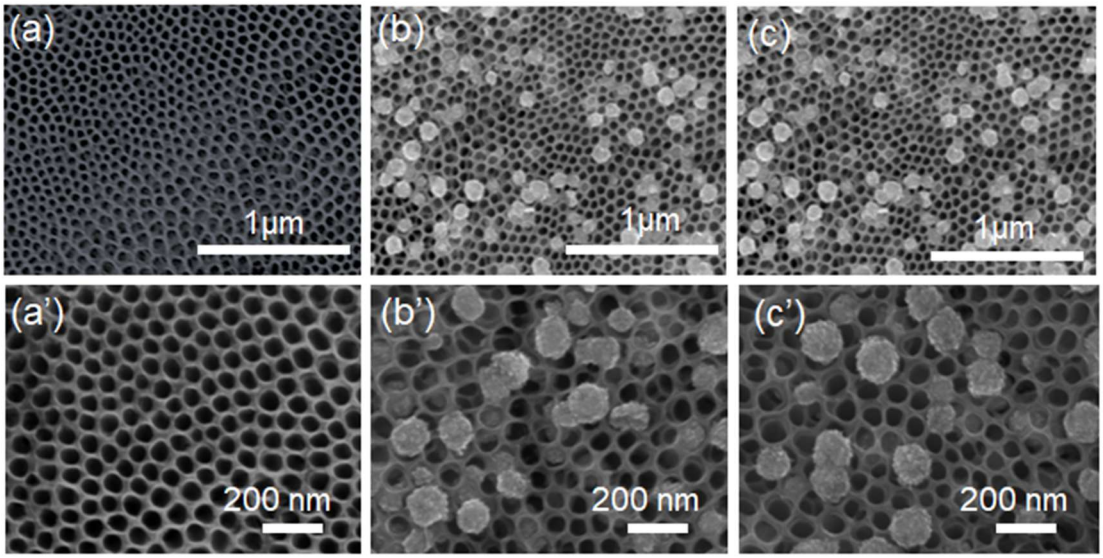


Figure 3. SEM images of T (**a**,**a'**), TN (**b**,**b'**), and TNC (**c**,**c'**) at different magnifications.

To further reveal the fine microstructure, lattice features, and elemental spatial distribution of the TNC photoanode, TEM, high-resolution TEM (HRTEM), and EDS elemental mapping were performed, as presented in Figure 4. The low-magnification TEM image (Figures 4a and S3a) reveals that granular NiO NPs (marked by green dashed circles) are homogeneously anchored on a porous TiO_2 nanotube scaffold. From the HRTEM image (Figure 4b), an interfacial boundary can be distinguished between the TiO_2 nanotubes and the loaded NiO NPs. The well-resolved lattice fringe with an interplanar spacing of 0.352 nm in Figure 4c corresponds to the (101) crystal plane of anatase TiO_2 [42–44], which is consistent with the XRD results described above. Meanwhile, lattice fringes of 0.209 nm and 0.241 nm (Figure 4d,e) are assigned to the (200) and (110) planes of cubic NiO [45,46], further confirming the successful growth of crystalline NiO domains on TiO_2 nanotubes. Notably, the edge regions outlined by white dashed lines in Figures 4b and S3b show no obvious lattice fringes and are most likely associated with the amorphous CoPi cocatalyst, consistent with its amorphous nature and in good accordance with our XRD observations and previous literature reports [47].

The high-angle annular dark-field scanning TEM (HAADF-STEM) image is shown in Figure 4f. The corresponding elemental mapping results (Figure 4g–k) display the spatial distribution of Ti, Ni, O, Co, and P elements. Ti and O elements are widely distributed over the whole framework, originating from the TiO_2 nanotube matrix. The Ni signal is concentrated in discrete nanoparticle regions, matching the location

of NiO NPs observed in HAADF-STEM. In addition, the Co and P signals are clearly observed in the elemental mapping, further confirming the successful deposition of CoPi on the TiO_2/NiO surface. Such a configuration, in which the CoPi cocatalyst is deposited on the TiO_2/NiO heterostructure, is expected to facilitate charge transfer across the TiO_2–NiO heterointerface and the semiconductor–cocatalyst interface, thereby promoting the PEC water splitting performance of the composite photoanode.

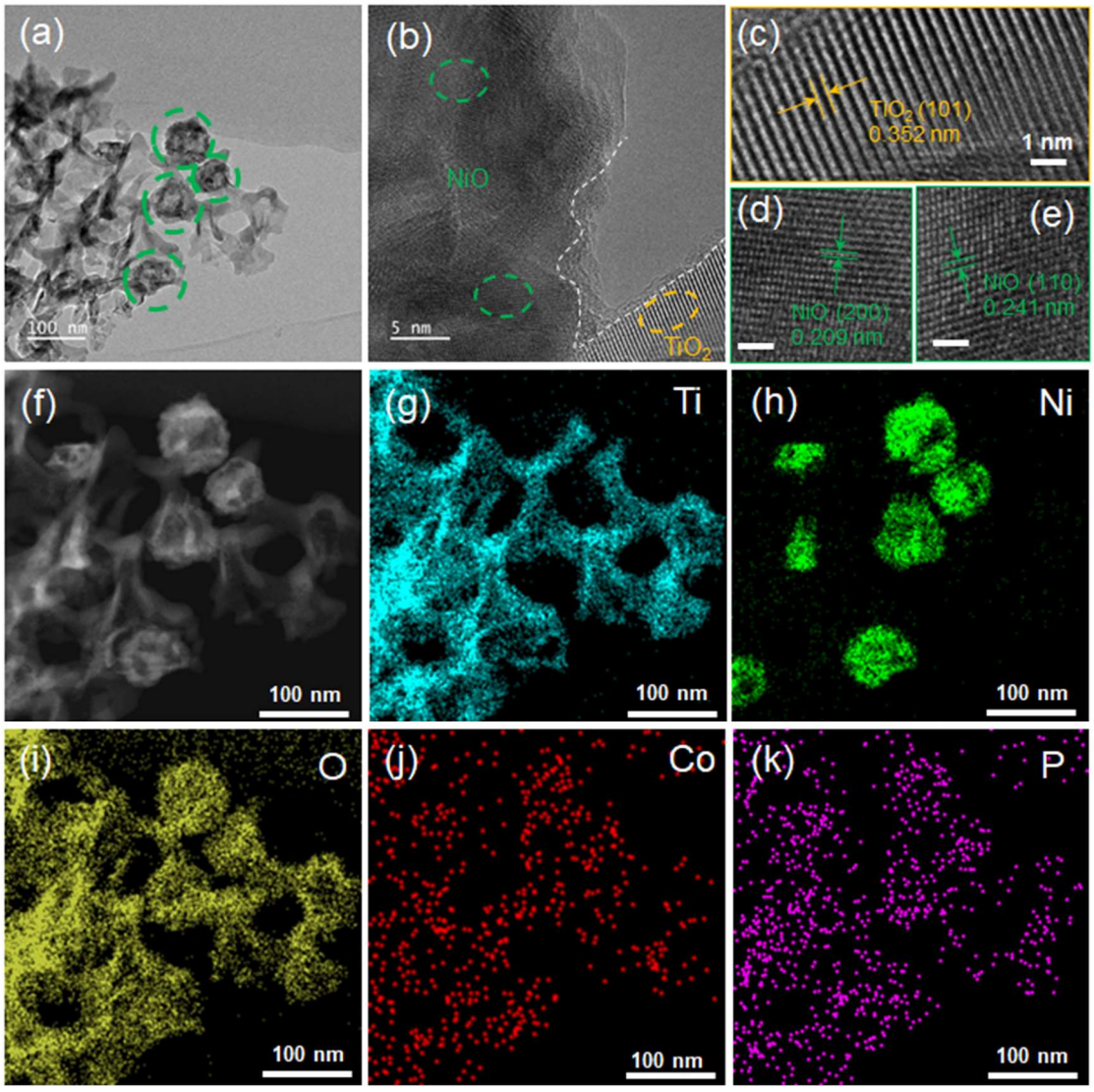


Figure 4. (**a**) TEM image of TNC electrode (green dashed circles represent NiO nanoparticles); (**b**–**e**) HRTEM images showing the lattice fringes of TiO_2 and NiO, the scale bars in panels (**c**–**e**) are all 1 nm; (**f**) HAADF-STEM image and corresponding EDS elemental mapping of (**g**) Ti, (**h**) Ni, (**i**) O, (**j**) Co, (**k**) P for TNC electrode.

3.3. Mott–Schottky Analysis and Optical Absorption

Mott–Schottky plots were recorded at 1000 Hz, a commonly used frequency for qualitatively assessing the semiconductor characteristics of photoelectrodes. As shown in Figure 5a, the T electrode exhibits a distinct positive slope in the potential range of −0.2 to 0.2 V *vs.* Ag/AgCl. Moreover, the slope does not turn negative as the potential increases further, demonstrating that the as-synthesized anatase TiO_2 nanotube arrays behave as a pure n-type semiconductor, consistent with previously reported results [48]. After NiO deposition, the M–S plot of TN displays a clear inverted "U-shape". When the potential exceeds 1.2 V, TN exhibits a p-type semiconducting feature originating from NiO, confirming the coexistence of n-type and p-type semiconductors in the TN electrode. This inverted-U profile is consistent with the characteristic

Mott–Schottky response of typical p-n heterojunctions [49–52]. Together with the above XRD, HRTEM, and XPS results, it indicates the formation of a p-n heterojunction within TN. Notably, TNC shows a similar M–S curve to TN, suggesting that CoPi loading does not significantly alter the semiconductor characteristics of the electrode.

The light-absorption capability of T, TN, and TNC electrodes was compared by UV-Vis DRS. As presented in Figure 5b, bare T absorbs mainly in the UV region below 400 nm, originating from the intrinsic band-gap transition of TiO_2 [53]. Its weak apparent absorption in the visible region likely arises from photon-guided resonance and light scattering from the ordered nanotube array rather than intrinsic TiO_2 absorption. After incorporating NiO, both TN and TNC exhibit a distinct absorption extension into the visible region (400–800 nm), which is attributed to the visible-light response of NiO. Notably, TNC shows nearly identical visible-light absorption to TN, indicating that CoPi decoration barely alters the optical-absorption behavior of the photoanode. Therefore, the superior photoelectrochemical activity of TNC cannot be mainly attributed to enhanced light harvesting.

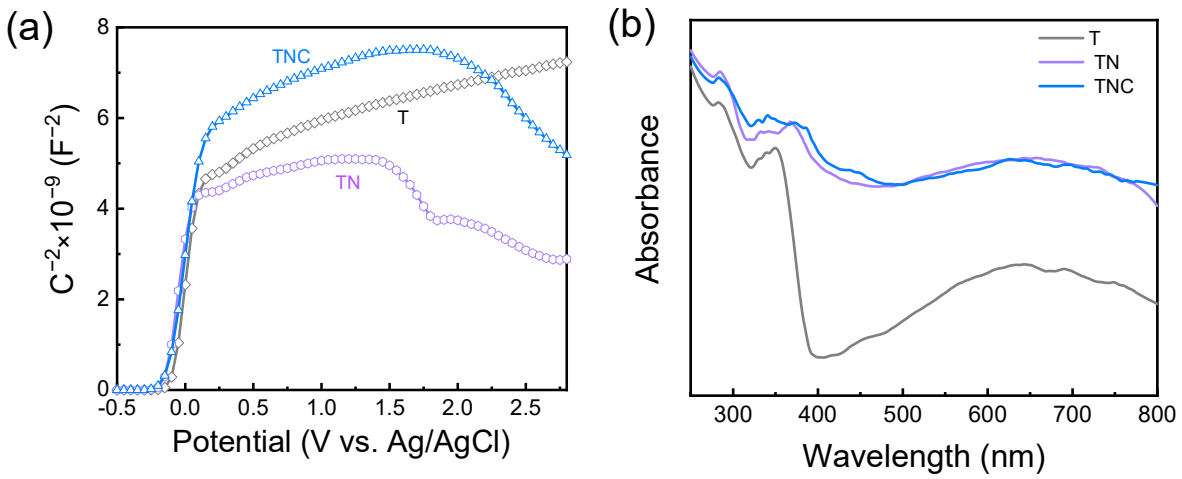


Figure 5. (**a**) Mott-Schottky plots of T, TN and TNC electrodes and (**b**) UV-Vis diffuse reflectance spectra.

3.4. Photoelectrochemical Performance and Charge Separation

The PEC performance of T, TN, and TNC photoanodes was systematically characterized by transient photocurrent, LSV, and EIS measurements. The transient photocurrent–time curves recorded at 0.6 V *vs.* Ag/AgCl (Figure 6a) show that all electrodes exhibit rapid and reversible responses to chopped illumination, with the photocurrent density following the order T < TN < TNC. The TNC photoanode produced the highest photocurrent density, with a steady-state value of 0.06 mA cm^{-2}, which was considerably higher than those of TN and T. Notably, the TC electrode (TiO_2 directly modified with CoPi without NiO) only exhibits a marginal increase in photocurrent density compared to bare T (Figure S4). This demonstrates that introducing CoPi alone contributes limited PEC activity, whereas the remarkable performance of TNC originates from the synergistic effect between the TiO_2/NiO heterojunction and the CoPi cocatalyst. The LSV curves under AM 1.5G illumination (Figure 6b) further confirm the superior performance of TNC, which exhibits the highest photocurrent density over the entire potential range measured. The stability of the TNC photoanode was evaluated by continuous chronoamperometry over 2 h in 0.1 M Na_2SO_4 (Figure S5). The photocurrent exhibits a gradual decay in the initial stage before reaching a steady plateau. The initial photocurrent decay is due to the accumulation of surface holes and the structural equilibration of CoPi in the non-buffered electrolyte [54].

For a more objective evaluation of the advantages of TNC, a comparison of photocurrent enhancement for various photoanodes modified with cocatalysts is summarized in Table S1. The photocurrent enhancement is defined as the ratio of the photocurrent density of the cocatalyst-modified electrode to that

of the electrode before cocatalyst modification. This metric directly reflects the effectiveness of cocatalyst loading while excluding the variations caused by different testing conditions (e.g., light sources, electrolyte pH, and applied potentials). As shown, the TNC photoanode achieves a remarkable 2.4-fold enhancement in photocurrent density after CoPi modification. This enhancement is highly competitive and even superior to many reported electrodes.

To further probe the interfacial charge-transfer kinetics, EIS measurements were performed in the dark and under illumination (Figure 6c). The semicircle diameter in the Nyquist plots represents the interfacial charge-transfer resistance (R_{ct}); a smaller semicircle corresponds to faster charge transfer [37,55–59]. It should be noted that the Nyquist semicircles appear incomplete within the measured frequency range because of the relatively large R_{ct} of the electrodes, a feature common to TiO_2-based photoelectrodes [60,61]. The R_{ct} values were therefore obtained by fitting the full-frequency EIS data with an equivalent circuit rather than from the visual completeness of the semicircles. The fitted R_{ct} values (Figure 6d) follow the order TN-dark (2251 Ω) > TNC-dark (1435 Ω) > TN-light (1086 Ω) > TNC-light (395 Ω). TNC under illumination exhibited the smallest semicircle and the lowest R_{ct} value. In comparison with T and TN, the enhanced photocurrent response and the pronounced decrease in R_{ct} for TNC suggest a synergistic effect between the TiO_2/NiO heterojunction and the CoPi cocatalyst. The TiO_2/NiO heterojunction is considered to facilitate the separation of photogenerated electron–hole pairs, while the CoPi layer acts as a hole extraction layer that accelerates interfacial hole transfer to the electrolyte and suppresses charge recombination.

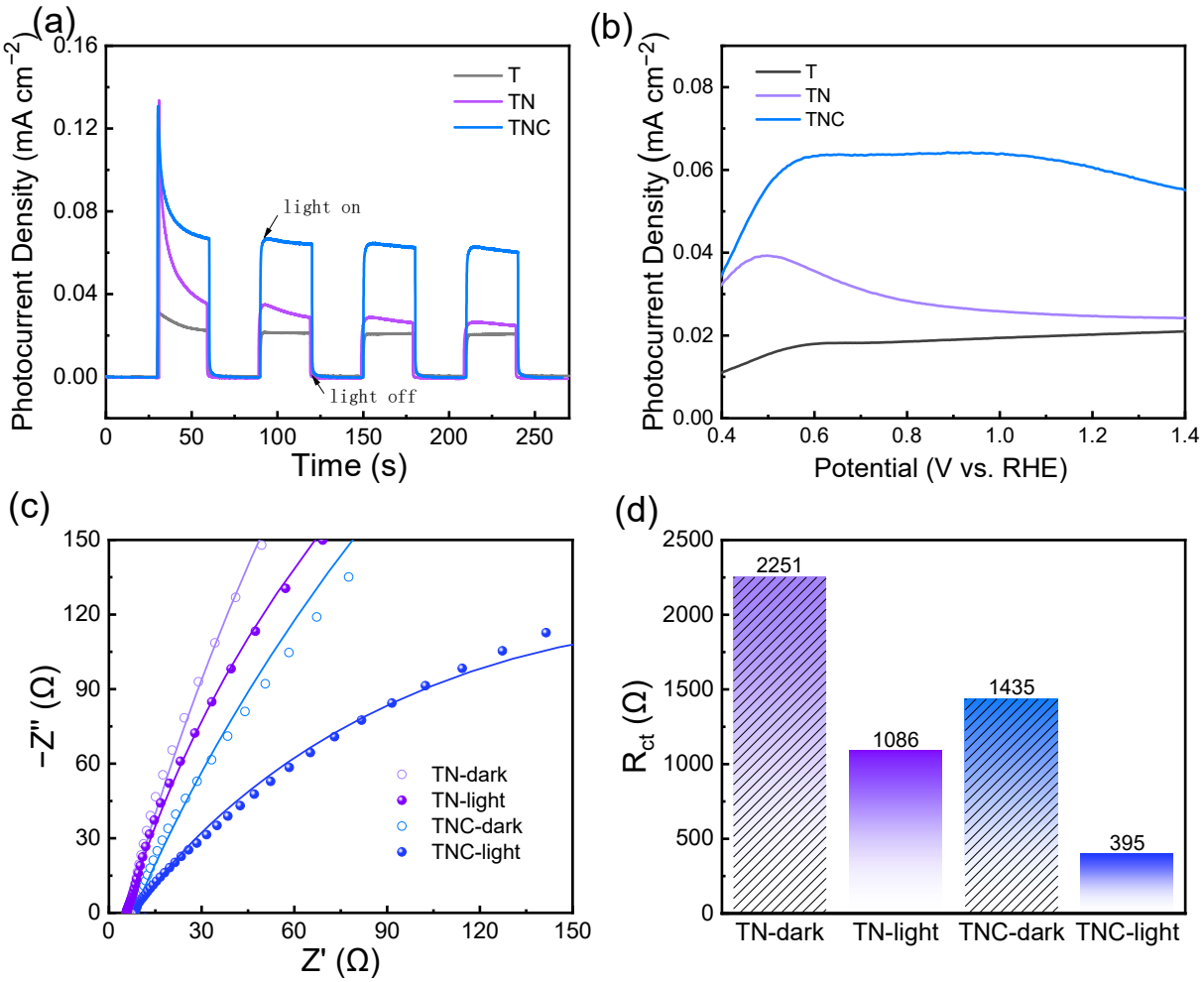


Figure 6. Photoelectrochemical performances of T, TN, and TNC photoanodes. (**a**) Photocurrent response under on-off light irradiation (AM 1.5G, 100 mW·cm^{-2}) at a bias voltage of 0.6 V *vs.* Ag/AgCl; (**b**) LSV curves under AM 1.5G illumination (*vs.*

RHE); (**c**) EIS Nyquist plots measured in dark and under illumination; (**d**) Fitted charge-transfer resistance (R_{ct}) values derived from EIS spectra.

OCP changes of T, TN and TNC photoanodes were measured, with the results shown in Figure 7a. The OCP curves for all electrodes are composed of three stages, containing the processes in the dark, under light-on and upon light-off. In the dark, the potential of each electrode is mainly governed by the equilibrium state at the semiconductor-electrolyte interface. Upon light irradiation, hole consumption at the semiconductor–electrolyte interface leads to the accumulation of photogenerated electrons within TiO_2, causing the Fermi level to shift toward more negative potentials [55,62]. Once photogeneration and recombination balance, the OCP reaches a stable maximum. Obviously, all three electrodes exhibit pronounced negative photopotential shifts. Relative to bare T, TN exhibits a much more negative steady-state OCP under illumination. NiO loading enhances charge separation and suppresses bulk recombination, increasing electron accumulation in TiO_2 and shifting the Fermi level negatively. TNC shows the most negative OCP. CoPi rapidly captures holes at the NiO surface, accelerating interfacial hole consumption, which further boosts electron accumulation and maximizes the photopotential shift. The OCP trend (T < TN < TNC) is consistent with the higher photocurrent and lower charge-transfer resistance of TNC, confirming that NiO and CoPi synergistically promote charge separation.

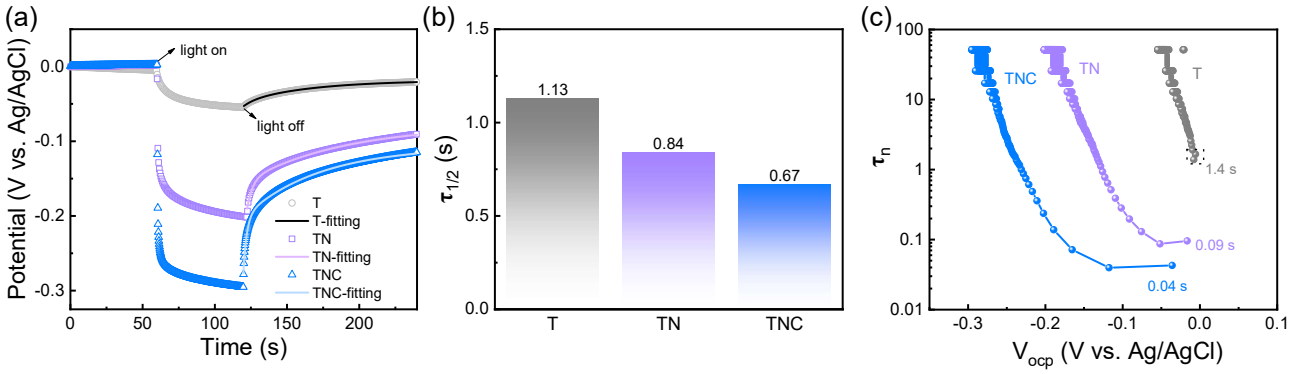


Figure 7. (**a**) Open-circuit potential (OCP) profiles and their fitting curves for T, TN and TNC photoanodes; (**b**) Half-decay carrier lifetime ($\tau_{1/2}$) extracted from OCP decay upon light-off; (**c**) Electron decay lifetime (τ_n) as a function of open-circuit potential.

After light-off, the photopotential decay was monitored to evaluate carrier recombination kinetics. Surface trap states can capture the charges transported to the electrode surface and hinder interfacial charge transfer between the photoanode and the electrolyte. A higher density of trap states generally results in a longer charge decay time. Accordingly, the OCP decay was fitted using a double-exponential equation (Equation (1)) to evaluate the surface trap states. Based on the fitted decay time constants τ_1 and τ_2, the harmonic average lifetime (τ_m) and the half-life of photopotential decay ($\tau_{1/2}$) were calculated using Equations (2) and (3) [63–65], respectively:

$$y_{(t)} = A_0 + A_1 e^{-t/\tau 1} + A_2 e^{-t/\tau 2} \quad (1)$$

$$\tau_m = {\tau_1 \tau_2}/{(\tau_1 + \tau_2)} \quad (2)$$

$$\tau_{1/2} = \tau_m \ln 2 \quad (3)$$

where A_0, A_1, A_2 are fitting constants. As presented in Figure 7b, bare T exhibits the $\tau_{1/2}$ (4.67 s) due to abundant surface trap states that hinder charge transfer. TiO_2/NiO heterojunction facilitates hole extraction toward NiO, suppressing trap-mediated capture and shortening $\tau_{1/2}$ to 2.38 s for TN. Further CoPi photodeposition passivates the trap states of the TNC electrode, enabling preferential hole transfer to CoPi

instead of recombination with electrons. This results in the shortest $\tau_{1/2}$ (1.6 s) for TNC. The progressive decrease in $\tau_{1/2}$ from T to TN to TNC indicates the stepwise optimization of interfacial charge dynamics by NiO and CoPi.

Furthermore, the apparent decay lifetime of the photogenerated carriers (τ_n) was estimated from the derivative of the OCP curve using Equations (4) [66,67]:

$$\tau_n = -\frac{k_B T}{e}\left(\frac{d\mathrm{OCP}}{dt}\right)^{-1} \quad (4)$$

where τ_n is the decay lifetime, k_B is the Boltzmann constant, T is the absolute temperature, and e is the positive element charge. The τ_n of TNC is obviously shorter than those of T and TN, which further confirms that the construction of the heterojunction and loading of CoPi cocatalyst effectively promote the extraction and transfer of photogenerated charge carriers and suppress charge recombination.

4. Conclusions

In summary, a CoPi cocatalyst-decorated TiO_2/NiO heterojunction photoanode was successfully constructed through two-step anodic oxidation of Ti sheets, NiO electrodeposition, and CoPi photodeposition. Cubic NiO nanoparticles were anchored on anatase TiO_2 nanotube arrays, while amorphous CoPi was homogeneously deposited on the TiO_2/NiO surface. This electrode design extended the photoresponse into the visible region from 400 to 800 nm and improved charge separation/interfacial hole transfer. The TNC photoanode exhibited the highest photocurrent density of 0.06 mA·cm^{-2} at steady state at 0.6 V *vs.* Ag/AgCl, the smallest charge-transfer resistance of 395 Ω under AM 1.5G illumination, the most significant open-circuit potential change, and the shortest carrier decay lifetime among T, TN, and TNC electrodes. The improved PEC water oxidation performance is attributed to the TiO_2/NiO heterojunction, which promotes charge separation, and the CoPi layer, which serves as a hole-extraction layer and passivates surface trap states.

Supplementary Materials

The following supporting information can be found at: https://www.sciepublish.com/article/pii/1330, Text S1: Detailed information on the chemicals and reagents used in this work; Text S2: Detailed characterization methods; Figure S1: High-resolution XPS spectra of the TN electrode (Ti 2p, Ni 2p, O 1s, P 2p and Co 2p); Figure S2: SEM image and corresponding EDS elemental mapping of O, Ti, Ni, Co and P for the TNC photoanode; Figure S3: TEM and HRTEM images of the TNC electrode; Figure S4: Transient photocurrent responses of the T and TC electrodes; Figure S5: Photocurrent stability of the TNC photoanode under continuous illumination over 7200 s; Table S1: Comparison of photocurrent enhancement of various photoanodes modified with different cocatalysts under AM 1.5G illumination.

Acknowledgments

We would like to thank the staff at the Analytical & Testing Center of Wuhan University of Science and Technology for their help with TEM analysis.

Author Contributions

Investigation, Data curation, Formal analysis, Writing—original draft, S.Z.; Investigation, Validation, H.C.; Investigation, Formal analysis, D.M.; Investigation, Validation, X.L.; Validation, Writing—review & editing, F.L.; Funding acquisition, Investigation, Z.W.; Investigation, Formal analysis, Q.K.; Conceptualization, Funding acquisition, Project administration, Supervision, Writing—review & editing, L.W.

Ethics Statement

Not applicable.

Informed Consent Statement

Not applicable.

Data Availability Statement

The data presented in this study are available on request from the corresponding author.

Funding

This work was financially supported by the Science and Technology Innovation Program of the General Administration of Sport of China (24KJCX077).

Declaration of Competing Interest

The authors declare that they have no known competing financial interests or personal relationships that could have appeared to influence the work reported in this paper.

References

1. Wang L, Huang J, Huang Z, Li H, Taylor Isimjan T, Yang X. Revealing dynamic structural evolution of V and P co-doping-induced Co defects as large-current water oxidation catalyst. *Chem. Eng. J.* **2023**, *472*, 144924. DOI:10.1016/j.cej.2023.144924
2. Fu S, Peng C, Luo Y, Cheng L, Yang X, Jiao Z. Modulating space charge of FeP/CoP p-n heterojunction for boosting oxygen evolution reaction. *J. Colloid Interface Sci.* **2024**, *664*, 349–359. DOI:10.1016/j.jcis.2024.03.060
3. Hu J, Al-Salihy A, Wang J, Li X, Fu Y, Li Z, et al. Improved interface charge transfer and redistribution in CuO-CoOOH p-n heterojunction nanoarray electrocatalyst for enhanced oxygen evolution reaction. *Adv. Sci.* **2021**, *8*, 2103314. DOI:10.1002/advs.202103314
4. Rani S, Roy SC, Paulose M, Varghese OK, Mor GK, Kim S, et al. Synthesis and applications of electrochemically self-assembled titania nanotube arrays. *Phys. Chem. Chem. Phys.* **2010**, *12*, 2780–2800. DOI:10.1039/b924125f
5. Xu SY, Shi W, Huang JR, Yao S, Wang C, Lu TB, et al. Single-cluster functionalized TiO_2 nanotube array for boosting water oxidation and CO_2 photoreduction to CH_3OH. *Angew. Chem. Int. Ed.* **2024**, *63*, e202406223. DOI:10.1002/anie.202406223
6. Xu Z, Zhang S, Gao F, Gao P, Yu Y, Lin J, et al. Enhanced charge separation and interfacial charge transfer of InGaN nanorods/C_3N_4 heterojunction photoanode. *Electrochim. Acta* **2019**, *324*, 134844. DOI:10.1016/j.electacta.2019.134844
7. Ji H, Du P, Zhao D, Li S, Sun F, Duin EC, et al. 2D/1D graphitic carbon nitride/titanate nanotubes heterostructure for efficient photocatalysis of sulfamethazine under solar light: Catalytic “hot spots” at the rutile-anatase-titanate interfaces. *Appl. Catal. B Environ.* **2020**, *263*, 118357. DOI:10.1016/j.apcatb.2019.118357
8. Ji H, Ni J, Zhao D, Liu W. Application of titanate nanotubes for photocatalytic decontamination in water: Challenges and prospects. *ACS ES&T Eng.* **2022**, *2*, 1015–1038. DOI:10.1021/acsestengg.1c00451
9. You P, Chen D, Liu X, Zhang C, Selloni A, Meng S. Correlated electron–nuclear dynamics of photoinduced water dissociation on rutile TiO_2. *Nat. Mater.* **2024**, *23*, 1100–1106. DOI:10.1038/s41563-024-01900-5
10. Jiang MP, Huang KK, Liu JH, Wang D, Wang Y, Wang X, et al. Magnetic-field-regulated TiO_2 {100} facets: A strategy for C-C coupling in CO_2 photocatalytic conversion. *Chem* **2020**, *6*, 2335–2346. DOI:10.1016/j.chempr.2020.06.033
11. Katal R, Masudy-Panah S, Tanhaei M, Farahani MHDA, Hu J. A review on the synthesis of the various types of anatase TiO_2 facets and their applications for photocatalysis. *Chem. Eng. J.* **2020**, *384*, 123384. DOI:10.1016/j.cej.2019.123384
12. Ren S, Hao H, Fan Y, Li J, Tian F, Liu J, et al. Construction of atomically dispersed Ni on tensile-strained TiO_2 for enhanced photocatalytic reduction of CO_2 to HCOOH. *Adv. Funct. Mater.* **2026**, *36*, e15558. DOI:10.1002/adfm.202515558
13. Hisatomi T, Yamada T, Nishiyama H, Takata T, Domen K. Materials and systems for large-scale photocatalytic water splitting. *Nat. Rev. Mater.* **2025**, *10*, 769–782. DOI:10.1038/s41578-025-00823-0
14. Kang U, Mizuochi R, Park H, Maeda K. Photoelectrochemical water oxidation using cobalt phosphate-modified nitrogen-doped titania nanotube arrays. *Small Struct.* **2023**, *4*, 2200229. DOI:10.1002/sstr.202200229

15. Li G, Wu L, Li F, Xu P, Zhang D, Li H. Photoelectrocatalytic degradation of organic pollutants via a CdS quantum dots enhanced TiO_2 nanotube array electrode under visible light irradiation. *Nanoscale* **2013**, *5*, 2118–2125. DOI:10.1039/c3nr34253k
16. Wu L, Li F, Xu Y, Zhang JW, Zhang D, Li G, et al. Plasmon-induced photoelectrocatalytic activity of Au nanoparticles enhanced TiO_2 nanotube arrays electrodes for environmental remediation. *Appl. Catal. B Environ.* **2015**, *164*, 217–224. DOI:10.1016/j.apcatb.2014.09.029
17. Shao Z, Ye C, Zhang Y, Wu Y, Xiong J, Li MMJ, et al. Epitaxial active interface to construct intralattice-bonded asymmetric Bi_1-O-Bi_2 sites for robust CO_2 photoreduction to acetic acid. *Angew. Chem. Int. Ed.* **2026**, *65*, e24970. DOI:10.1002/anie.202524970
18. Shao Z, Ye C, Zhang Y, Xiong J, Zuo H, Jiang W, et al. Interfacial differentiated recoordination trigger asymmetric Bi (δ^+)-Bi (δ^-) regions for robust CO_2 photosynthesis to CH_3COOH. *Adv. Mater.* **2026**, *38*, e73924. DOI:10.1002/adma.73924
19. Chen L, Gu Q, Hou L, Zhang C, Lu Y, Wang X, et al. Molecular p–n heterojunction-enhanced visible-light hydrogen evolution over a N-doped TiO_2 photocatalyst. *Catal. Sci. Technol.* **2017**, *7*, 2039–2049. DOI:10.1039/c7cy00495h
20. Parvizi T, Parsa JB, Farnood R. Highly-efficient degradation of organic pollutants and synchronous electricity generation in a photocatalytic fuel cell based on the catalytic reactions of hydroxyl and chlorine radicals. *Electrochim. Acta* **2021**, *370*, 137753. DOI:10.1016/j.electacta.2021.137753
21. Liu J, Li Y, Ke J, Wang S, Wang L, Xiao H. Black NiO-TiO_2 nanorods for solar photocatalysis: Recognition of electronic structure and reaction mechanism. *Appl. Catal. B Environ.* **2018**, *224*, 705–714. DOI:10.1016/j.apcatb.2017.11.028
22. Shen G, Zhang R, Pan L, Hou F, Zhao Y, Shen Z, et al. Regulating the spin state of Fe^{III} by atomically anchoring on ultrathin titanium dioxide for efficient oxygen evolution electrocatalysis. *Angew. Chem. Int. Ed.* **2020**, *59*, 2313–2317. DOI:10.1002/anie.201913080
23. He B, Cao Y, Lin K, Wang Y, Li Z, Yang Y, et al. Strong interactions between Au nanoparticles and $BiVO_4$ photoanode boosts hole extraction for photoelectrochemical water splitting. *Angew. Chem. Int. Ed.* **2024**, *63*, e202402435. DOI:10.1002/anie.202402435
24. Jiang L, Chen X, Jiang L, Luo X, Li R, Zhou Q, et al. Oxyanion-triggered discrepant oxide pathways via tailoring reconstruction of non-noble catalysts for water oxidation. *Nano Lett.* **2025**, *25*, 13875–13884. DOI:10.1021/acs.nanolett.5c03709
25. Qi J, Lin YP, Chen D, Zhou T, Zhang W, Cao R. Autologous cobalt phosphates with modulated coordination sites for electrocatalytic water oxidation. *Angew. Chem.* **2020**, *132*, 9002–9006. DOI:10.1002/ange.202001737
26. Ma Y, Kafizas A, Pendlebury SR, Le Formal F, Durrant JR. Photoinduced absorption spectroscopy of CoPi on $BiVO_4$: The function of CoPi during water oxidation. *Adv. Funct. Mater.* **2016**, *26*, 4951–4960. DOI:10.1002/adfm.201600711
27. Bu Q, Li S, Zhang K, Lin Y, Wang D, Zou X, et al. Hole transfer channel of ferrihydrite designed between Ti–Fe_2O_3 and CoPi as an efficient and durable photoanode. *ACS Sustain. Chem. Eng.* **2019**, *7*, 10971–10978. DOI:10.1021/acssuschemeng.9b02009
28. Ma Y, Le Formal F, Kafizas A, Pendlebury SR, Durrant JR. Efficient suppression of back electron/hole recombination in cobalt phosphate surface-modified undoped bismuth vanadate photoanodes. *J. Mater. Chem. A* **2015**, *3*, 20649–20657. DOI:10.1039/c5ta05826k
29. Song R, Hu X, Zhang L, Wang X, Wang H, Chi H, et al. Boosting the photoelectrocatalytic degradation kinetics of phenolic compounds on a TiO_2 photoanode by loading the NiO cocatalyst. *ACS Catal.* **2025**, *15*, 4942–4952. DOI:10.1021/acscatal.5c00638
30. Roy P, Berger S, Schmuki P. TiO_2 nanotubes: Synthesis and applications. *Angew. Chem. Int. Ed.* **2011**, *50*, 2904–2939. DOI:10.1002/anie.201001374
31. Shaik S, Kim J, Kabiraz MK, Aziz F, Park JY, Anne BR, et al. Rapid outgassing of hydrophilic TiO_2 electrodes achieves long-term stability of anion exchange membrane water electrolyzers. *Nano-Micro Lett.* **2025**, *17*, 186. DOI:10.1007/s40820-025-01696-2
32. Kim TW, Choi KS. Nanoporous $BiVO_4$ photoanodes with dual-layer oxygen evolution catalysts for solar water splitting. *Science* **2014**, *343*, 990–994. DOI:10.1126/science.1246913
33. Yu Y, Zhang Z, Yin X, Kvit A, Liao Q, Kang Z, et al. Enhanced photoelectrochemical efficiency and stability using a conformal TiO_2 film on a black silicon photoanode. *Nat. Energy* **2017**, *2*, 17045. DOI:10.1038/nenergy.2017.45
34. Tian Z, Zhang P, Qin P, Sun D, Zhang S, Guo X, et al. Novel black $BiVO_4/TiO_{2-x}$ photoanode with enhanced photon absorption and charge separation for efficient and stable solar water splitting. *Adv. Energy Mater.* **2019**, *9*, 1901287. DOI:10.1002/aenm.201901287
35. Liu L, Luo S, Lu WN, Song H, Lin H, Li S, et al. Defective TiO_x sublayers break the activity–stability trade-off for green flexible water photoelectrolysis. *ACS Nano* **2026**, *20*, 358–369. DOI:10.1021/acsnano.5c12657

36. Chen L, Song XL, Ren JT, Yuan ZY. Precisely modifying Co_2P/black TiO_2 S-scheme heterojunction by in situ formed P and C dopants for enhanced photocatalytic H_2 production. *Appl. Catal. B Environ.* **2022**, *315*, 121546. DOI:10.1016/j.apcatb.2022.121546
37. Li H, Zhu Z, Zhang S, Chen X, Cao Y, Wang M, et al. Co-Ni sulfides embedded in yolk-shell carbon matrix for efficient peroxymonosulfate activation and suppressed metal leaching toward atrazine degradation. *Sep. Purif. Technol.* **2026**, *405*, 138938. DOI:10.1016/j.seppur.2026.138938
38. Zhang B, Sun B, Liu X, Liu W, Gu S, Zhou G. Defect-engineered S-scheme charge transfer in $TiO_2/Zn_{0.5}Cd_{0.5}S$ heterojunction for high-efficiency photocatalytic hydrogen evolution. *Chin. J. Catal.* **2026**, *84*, 117–129. DOI:10.1016/S1872-2067(25)64909-6
39. Zhang Y, Feng H, Song Y, Yu S, Zhang C, Feng Y, et al. Anion-driven oxygen configuration tuning on NiO boosts hydrogen peroxide production. *Appl. Catal. B Environ. Energy* **2026**, *384*, 126156. DOI:10.1016/j.apcatb.2025.126156
40. Lan D, Pang F, Ge J. Enhanced charge separation in NiO and Pd Co-modified TiO_2 photocatalysts for efficient and selective photoreduction of CO_2. *ACS Appl. Energy Mater.* **2021**, *4*, 6324–6332. DOI:10.1021/acsaem.1c01144
41. Li M, Yang J, Li S, Deng L, Zhao S, Li L, et al. Rare-earth-induced intermediate-spin Co centers in $MnCo_2O_{4.5}$ for sustainable acidic water oxidation. *J. Am. Chem. Soc.* **2025**, *147*, 45680–45690. DOI:10.1021/jacs.5c17361
42. Utomo WP, Wu H, Ng YH. Modulating the active sites of oxygen-deficient TiO_2 by copper loading for enhanced electrocatalytic nitrogen reduction to ammonia. *Small* **2022**, *18*, 2200996. DOI:10.1002/smll.202200996
43. Zheng Z, Zhang C, Li J, Fang D, Tan P, Fang Q, et al. Insight into the effect of exposed crystal facets of anatase TiO_2 on HCHO catalytic oxidation of Mn-Ce/TiO_2. *J. Hazard. Mater.* **2024**, *474*, 134710. DOI:10.1016/j.jhazmat.2024.134710
44. Chang Y, Li P, Zhao T, Wang H, Wang F, Lin C, et al. Boosting photocatalytic activity through dual functionalization: Oxygen vacancy-rich 2D mesoporous TiO_2 nanosheets integrated with bimetallic nanoclusters. *Adv. Funct. Mater.* **2025**, *35*, e14365. DOI:10.1002/adfm.202514365
45. Wang D, Li Q, Miao W, Liu Y, Du N, Mao S. One-pot synthesis of ultrafine NiO loaded and Ti^{3+} in-situ doped TiO_2 induced by cyclodextrin for efficient visible-light photodegradation of hydrophobic pollutants. *Chem. Eng. J.* **2020**, *402*, 126211. DOI:10.1016/j.cej.2020.126211
46. Duan L, Quan X, Du R, Chen G, Liu M, Liu X, et al. Oxygen-bridge-mediated NiO/WO_3 heterostructure for highly efficient electrocatalytic nitrate-to-ammonia conversion. *Adv. Funct. Mater.* **2026**, *36*, e75297. DOI:10.1002/adfm.75297
47. Liang J, Li Z, Zhang M, Wang H, Cai Z, Luo Y, et al. Amorphous phosphates tailor local proton supply for alkaline hydrogen evolution electrocatalysis. *Adv. Mater.* **2025**, *37*, 2503660. DOI:10.1002/adma.202503660
48. Tanaka A, Teramura K, Hosokawa S, Kominami H, Tanaka T. Visible light-induced water splitting in an aqueous suspension of a plasmonic Au/TiO_2 photocatalyst with metal co-catalysts. *Chem. Sci.* **2017**, *8*, 2574–2580. DOI:10.1039/c6sc05135a
49. Wang H, Hu YL, Song GL, Zheng DJ. Intrinsic and extrinsic doping to construct hematite nanorod p-n homojunctions for highly efficient PEC water splitting. *Chem. Eng. J.* **2022**, *435*, 135016. DOI:10.1016/j.cej.2022.135016
50. Kim E, Kim S, Kim Y, Hamkins K, Baek J, Kim M, et al. Activation of hidden catalytic sites in 2D basal plane via p–n heterojunction interface engineering toward efficient oxygen evolution reaction. *Adv. Energy Mater.* **2025**, *15*, 2403722. DOI:10.1002/aenm.202403722
51. Liu Z, Wang L, Yu X, Zhang J, Yang R, Zhang X, et al. Piezoelectric-effect-enhanced full-spectrum photoelectrocatalysis in p–n heterojunction. *Adv. Funct. Mater.* **2019**, *29*, 1807279. DOI:10.1002/adfm.201807279
52. Kuchayita KK, Su WN, Cheng CC. Unleashing the power of P-N heterojunctions: Optimizing water electrolysis efficiency through a cathode-driven electrocatalyst synergy. *Adv. Sci.* **2026**, *13*, e75398. DOI:10.1002/advs.75398
53. Yu H, Wang M, Yan J, Dang H, Zhu H, Liu Y, et al. Complete mineralization of phenolic compounds in visible-light-driven photocatalytic ozonation with single-crystal WO_3 nanosheets: Performance and mechanism investigation. *J. Hazard. Mater.* **2022**, *433*, 128811. DOI:10.1016/j.jhazmat.2022.128811
54. Okazaki M, Suganami Y, Hirayama N, Nakata H, Oshikiri T, Yokoi T, et al. Site-selective deposition of a cobalt cocatalyst onto a plasmonic Au/TiO_2 photoanode for improved water oxidation. *ACS Appl. Energy Mater.* **2020**, *3*, 5142–5146. DOI:10.1021/acsaem.0c00857
55. Zhao Y, Li J, Han J, Fu GE, Zhang W, Chen T, et al. A coumarin-linked conjugated covalent organic framework for enhanced photocatalytic hydrogen evolution. *Nat. Synth.* **2026**, DOI:10.1038/s44160-026-01146-w
56. Hou K, Zhang S, Yin P, Liu T, Cao Y, Wang M, et al. Zinc vaporization induced formation of desired Ni nanoparticles coated with ultrathin carbon shells for efficient electrocatalytic H_2 production coupling with methanol upgrading. *ACS Appl. Mater. Interfaces* **2024**, *16*, 52326–52338. DOI:10.1021/acsami.4c10405
57. Xuan F, Li Y, Zhang S, Yang L, Lv F, Wang M, et al. Enteromorpha-derived Fe/N-rich carbon for efficient degradation of thiacloprid via catalytic ozonation. *Sep. Purif. Technol.* **2025**, *371*, 133441. DOI:10.1016/j.seppur.2025.133441

58. Zhang S, Chang H, Liu W, Cao Y, Zhan W, Wang R, et al. Ligand-to-cluster charge transfer enables efficient photocatalytic ozonation over a robust porphyrin-functionalized Fe-MOF. *Appl. Catal. B Environ. Energy* **2027**, *401*, 127385. DOI:10.1016/j.apcatb.2026.127385
59. Zhang S, Wu J, Yang S, Li H, Li Y, Wang M, et al. Round-the-clock degradation of pharmaceutical pollutants by photocatalytic and catalytic ozonation based on bifunctional MIL-100(Fe) catalyst. *Water Res.* **2025**, *284*, 124017. DOI:10.1016/j.watres.2025.124017
60. Ghosh D, Roy K, Maitra S, Kumar P. Synergistic spin-state modulation in Co/N co-doped TiO_2 for enhanced photoelectrocatalytic oxygen evolution under external magnetic fields. *J. Mater. Chem. A* **2026**, *14*, 24725–24735. DOI:10.1039/d6ta00083e
61. Sun Y, Tian R, Niu L, Sun Y, Zhang W, Wang H, et al. TiO_2 nanorod arrays modified by AuAg alloy nanoparticles for photoelectrocatalytic glycerol conversion and synergistic hydrogen production. *Int. J. Hydrogen Energy* **2025**, *119*, 34–44. DOI:10.1016/j.ijhydene.2025.03.220
62. Chen Z, Wu S, Ma J, Mine S, Toyao T, Matsuoka M, et al. Non-oxidative coupling of methane: N-type doping of niobium single atoms in TiO_2–SiO_2 induces electron localization. *Angew. Chem. Int. Ed.* **2021**, *60*, 11901–11909. DOI:10.1002/anie.202016420
63. Tang R, Wang L, Ying M, Yang W, Kheradmand A, Jiang Y, et al. Multigraded heterojunction hole extraction layer of ZIF-Co_xZn_{1-x} on Co_3O_4/TiO_2 skeleton for a new photoanode architecture in water oxidation. *Small Sci.* **2021**, *1*, 2000033. DOI:10.1002/smsc.202000033
64. Leil R, Abodouh MM, Javed N, Sreekumar S, Pacheco H, Tarek N, et al. Untapped potential of scrap brass alloy: A new frontier in the use of brass-based photocathodes for stable and durable photoelectrochemical water splitting. *Energy Adv.* **2024**, *3*, 430–441. DOI:10.1039/d3ya00534h
65. Xu C, Wang H, Liang K, Zhang Y, Li W, Zhang H. Inducing hollow and porous hematite nanorod photoanodes by rare earth and transition metal doping for enhanced solar water splitting. *J. Mater. Chem. A* **2024**, *12*, 11831–11840. DOI:10.1039/d4ta01258e
66. Zhong M, Hisatomi T, Kuang Y, Zhao J, Liu M, Iwase A, et al. Surface modification of CoO_x loaded $BiVO_4$ photoanodes with ultrathin p-type NiO layers for improved solar water oxidation. *J. Am. Chem. Soc.* **2015**, *137*, 5053–5060. DOI:10.1021/jacs.5b00256
67. He B, Cao Y, Lin K, Wu M, Zhu Y, Cui X, et al. Enhanced bulk and interfacial charge transfer in Fe:$VOPO_4$ modified Mo:$BiVO_4$ photoanodes for photoelectrochemical water splitting. *eScience* **2025**, *5*, 100242. DOI:10.1016/j.esci.2024.100242